**FIGURE 6.** Case 8, pleomorphic adenoma in the left parotid gland of a 52-year-old woman. A, T1W image [400/9 (TR/TE), axial plane] of the maximal diameter section shows a lobulated tumor of isointensity for muscle in the superficial lobe. B, Fat-suppressed T2W image (4000/100, axial plane) shows a homogeneous and markedly high-intensity mass. C, All of the tumor at the same level as T1W and fat-suppressed T2W images had type D perfusion curve on dynamic MR images. D, Maximal diameter axial section of the specimen shows abundant myxoid components.

All portions of the tumor showed type D perfusion curve on dynamic MR images. The medial half of the tumor showed marked delay enhancement. The region had a high ADC value $(1.79 \times 10^{-3}$ mm$^2$/s) on DW images, but had no characteristic high intensity on STIR images. The pathologic specimen revealed small nets and cords of carcinomatous ductal epithelium within abundant fibrous tissue stroma and variably sized foci of necrosis.

## DISCUSSION

It is important to determine whether a salivary gland tumor is benign or malignant and to assess the extent of a tumor

and the relationship with adjacent structures preoperatively, as this information strongly influences the surgical procedures. Benign tumors undergo local excision or superficial parotidectomy whereas total parotidectomy with or without facial nerve removal is performed for malignant tumors. Clinically, malignant tumors sometimes show facial nerve palsy due to encasement of the nerve. MR imaging is an established and useful way of demonstrating the morphology and extent of head and neck tumors, as well as their relationship with adjacent structures, prior to surgery. However, there is general agreement that MR imaging cannot make a confident distinction between benign and malignant neoplasms and that it is not particularly
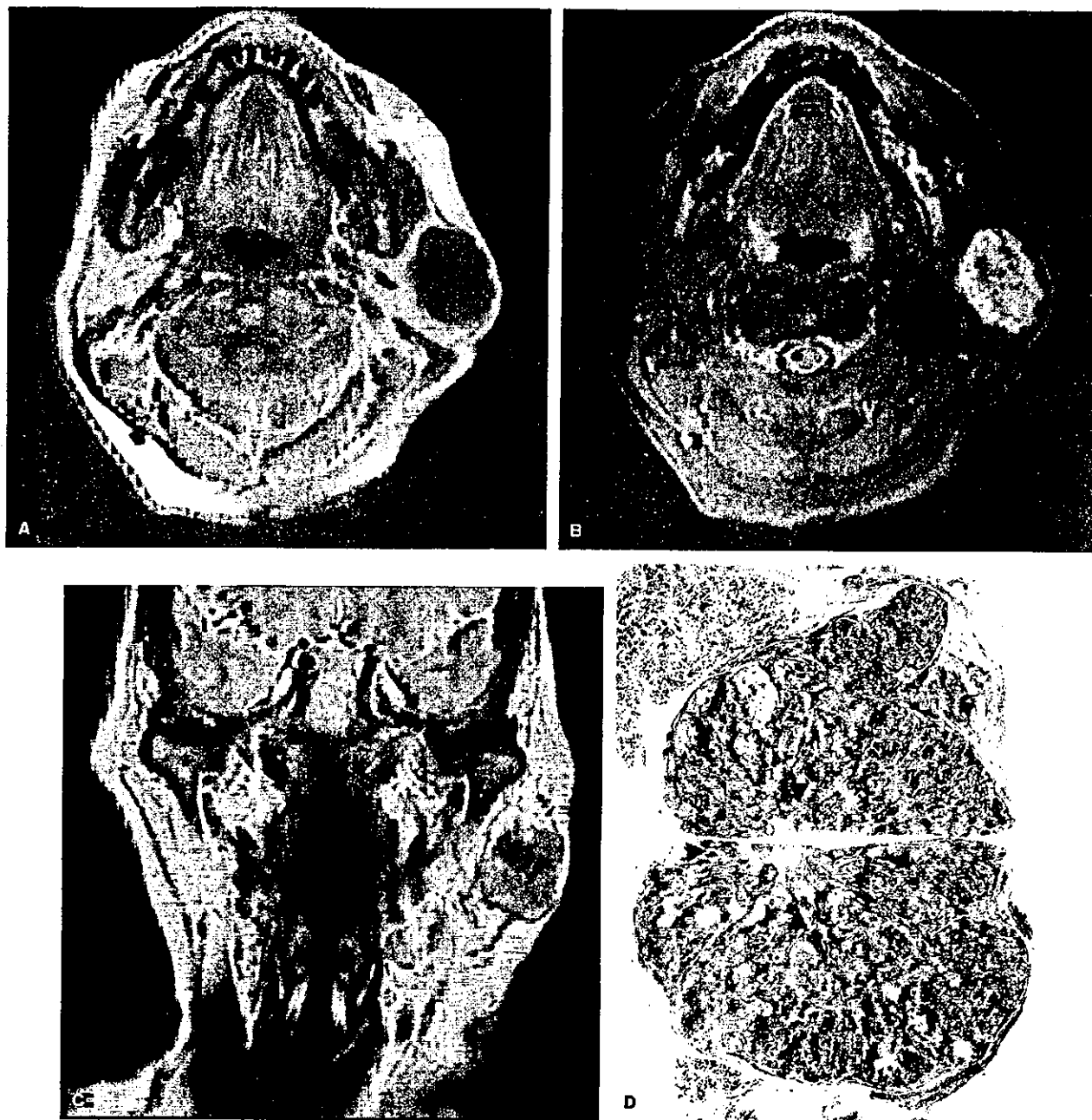
FIGURE 7. Case 27, pleomorphic adenoma in the left parotid gland of a 50-year-old woman. A, T1W image [400/9 (TR/TE), axial plane] shows a lobulated hypointensity tumor. B, STIR (4000/30, axial plane) shows high-intensity tumor. The tumor has an irregular and ill-defined area of lower intensity at the central region. The central hypointense region is also seen on T2W images. C, T2W image (4000/100, coronal plane) shows a lobulated tumor with hypointensity rim. The tumor has isointensity to gray matter with hypointensity area at the central region. D, The central hypointensity region on STIR and T2W images represents fibrosis (arrowheads). The remaining region is composed of many hypercellular and myxoid nests.

useful for a pathologic diagnosis.[6,8,11–17] These previous studies were based on combinations of conventional MR sequences, T1W, T2W, and gadolinium-enhanced MR images or dynamic MR imaging alone or DW imaging alone. There was

no study that provided variable MR imaging of parotid tumors with emphasis on the role of dynamic MR imaging and DW images. According to Yabuuchi et al,[13] in a study including 22 benign and 11 malignant tumors, gadolinium-enhanced dy-
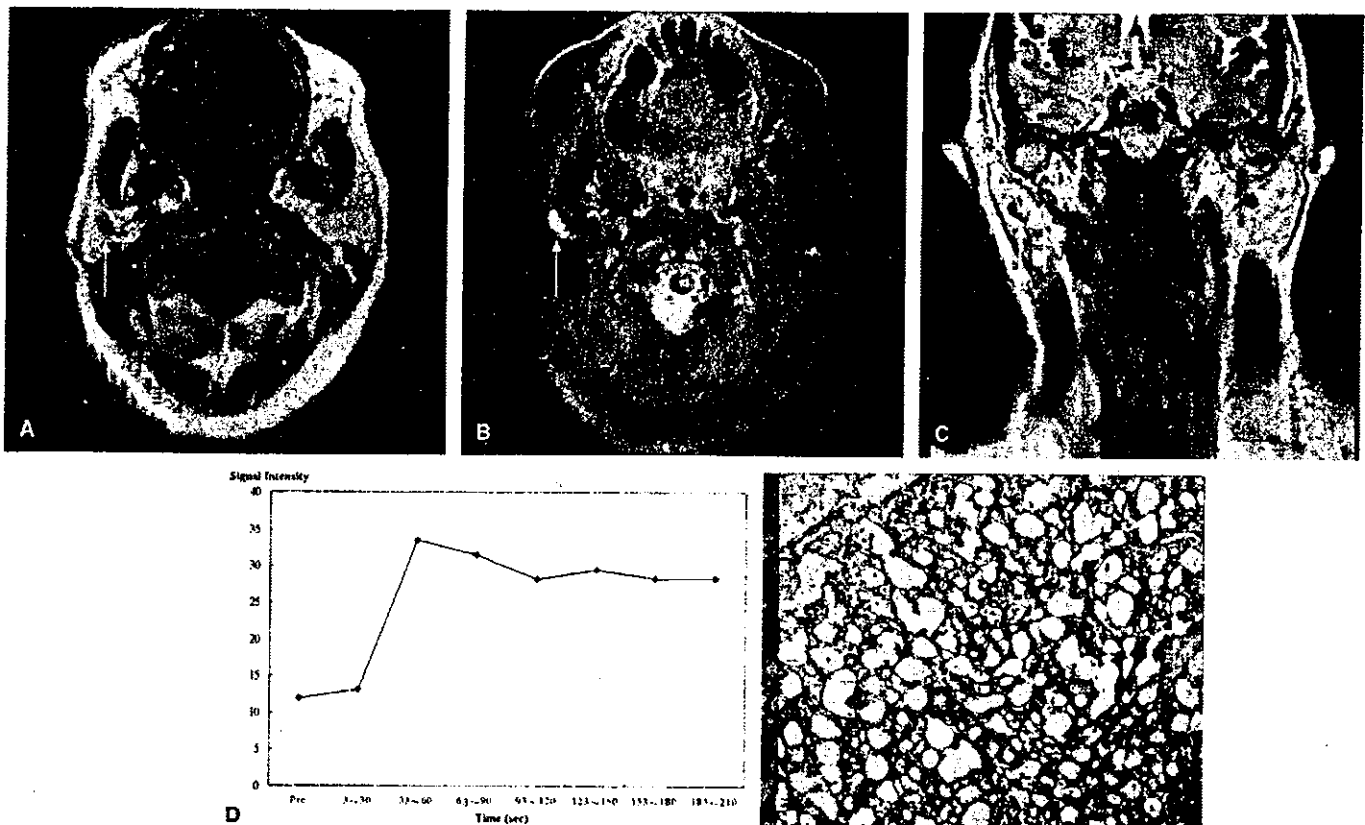
**FIGURE 8.** Acinic cell adenocarcinoma in the right parotid gland of a 61-year-old woman. A, T1W image [400/9 (TR/TE), axial plane] of the maximal diameter section shows a small oval-shaped tumor. B, STIR (4000/30, axial plane) shows marked high-intensity tumor. C, T2W image (4000/100, coronal plane) shows moderate high-intensity tumor. D, This tumor has type A perfusion curve on dynamic MR images. E, The pathologic specimen revealed numerous small cysts interspersed among epithelial tumor cells. Some areas demonstrated solid growth.

namic MR imaging was useful for predicting whether salivary gland tumors are benign or malignant. Parotid tumors can be diagnosed primarily by a clinical examination carried out by an experienced clinician and by FNAC. FNAC is probably the most economical and minimally invasive way to diagnose a parotid tumor, but its results are not always conclusive because insufficient specimens are sometimes obtained due to small sample size or deep tumor location.[18,19] FNAC of the tumor risks spillage and dramatically increases the risk of recurrence,[1-4] meaning that resection of the soft tissue penetrated by the needle will be required. Therefore, preoperative imaging has an important role in the surgical planning for parotid tumors, both for determining whether a salivary gland tumor is benign or malignant and for assessing the extent of the tumor and the relationship with adjacent structures.

Pleomorphic adenoma (mixed tumor) is the most common benign neoplasm of salivary gland origin. The average age of patients with pleomorphic adenomas is about 43 years,[20] but this tumor is the most common neoplasm of the salivary gland even in children and adolescents. Women are more likely to be affected than men.[20] Pleomorphic adenoma is

usually solitary, round, and well circumscribed with a smooth but sometimes lobulated surface. Tumors larger than 1 cm often have numerous protuberances, which give them a lobulated appearance. In the major salivary glands, pleomorphic adenomas are commonly encapsulated, but in the minor glands they usually are not. The average maximal cross-sectional diameter of pleomorphic adenomas is 2.1 cm (1.0–5.4 cm).[8] In our study, the average age of patients with pleomorphic adenomas was 50 years, with a range of 15 to 70 years. Twenty-four patients were women and 9 were men. All cases had solitary pleomorphic adenomas. The average maximal cross-sectional diameter of pleomorphic adenomas in our study was 2.6 cm (1.0–5.8 cm). Our data agreed well with those of the previous articles.

Pleomorphic adenomas are renowned for their cytomorphological and architectural variability. Despite their protean histopathology, all tumors share the essential diagnostic features of being composed of both epithelial and myxoid tissues. The proportions of these components vary widely, and one or the other is often predominant.

Previous studies suggested that pleomorphic adenomas typically have a characteristic high intensity on T2W images,
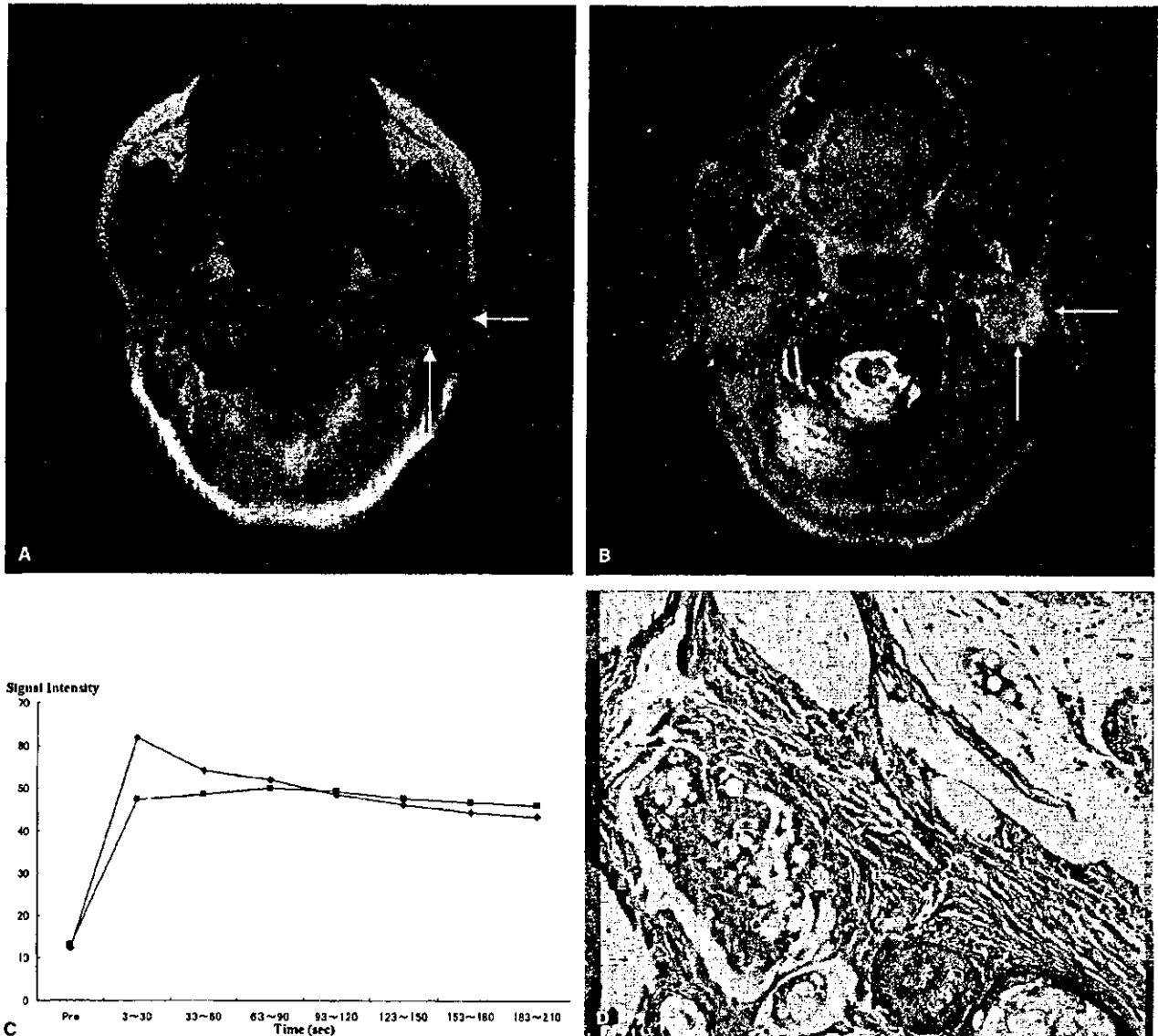
FIGURE 9. Mucoepidermoid carcinoma in the left parotid gland of a 60-year-old woman. A, T1W image [400/9 (TR/TE), axial plane] of the maximal diameter section shows a tumor with an ill-defined border of isointensity for muscle (arrows). The tumor shows invasive growth from deep to superficial lobe. B, STIR (4000/30, axial plane) shows iso to moderate high-intensity tumor (arrows). C, This tumor has 2 types of TICs on dynamic MR images: type A and C1 perfusion curves on dynamic MR images. D, The pathologic specimen revealed that more than 20% of this tumor was composed of cystic space. A large portion also demonstrated solid growth.

representing myxoid tissue.[4–10] In the current study, the characteristic bright signals with a higher intensity than that of bright CSF signals on STIR and T2W images were also found to represent myxoid-dominant tissue. STIR is sensitive to changes in T1 and T2 values, and an inversion time is chosen such that the signal intensity of fat is zero at the time of 90-degrees pulse, which produces an image with a higher net tissue contrast than that produced by T2-weighted spin-echo im-

age.[21] The STIR sequence has been shown to demonstrate increased conspicuity of lesions compared with T2-weighted images. The intensity of the pleomorphic adenoma on STIR and T2W images was not always homogeneous. We speculated that the cellular component with less-myxoid tissue was responsible for the reduced signal intensities on STIR and T2W images, with the reduction ratio being dependent on the proportion of cellular components. The myxoid component
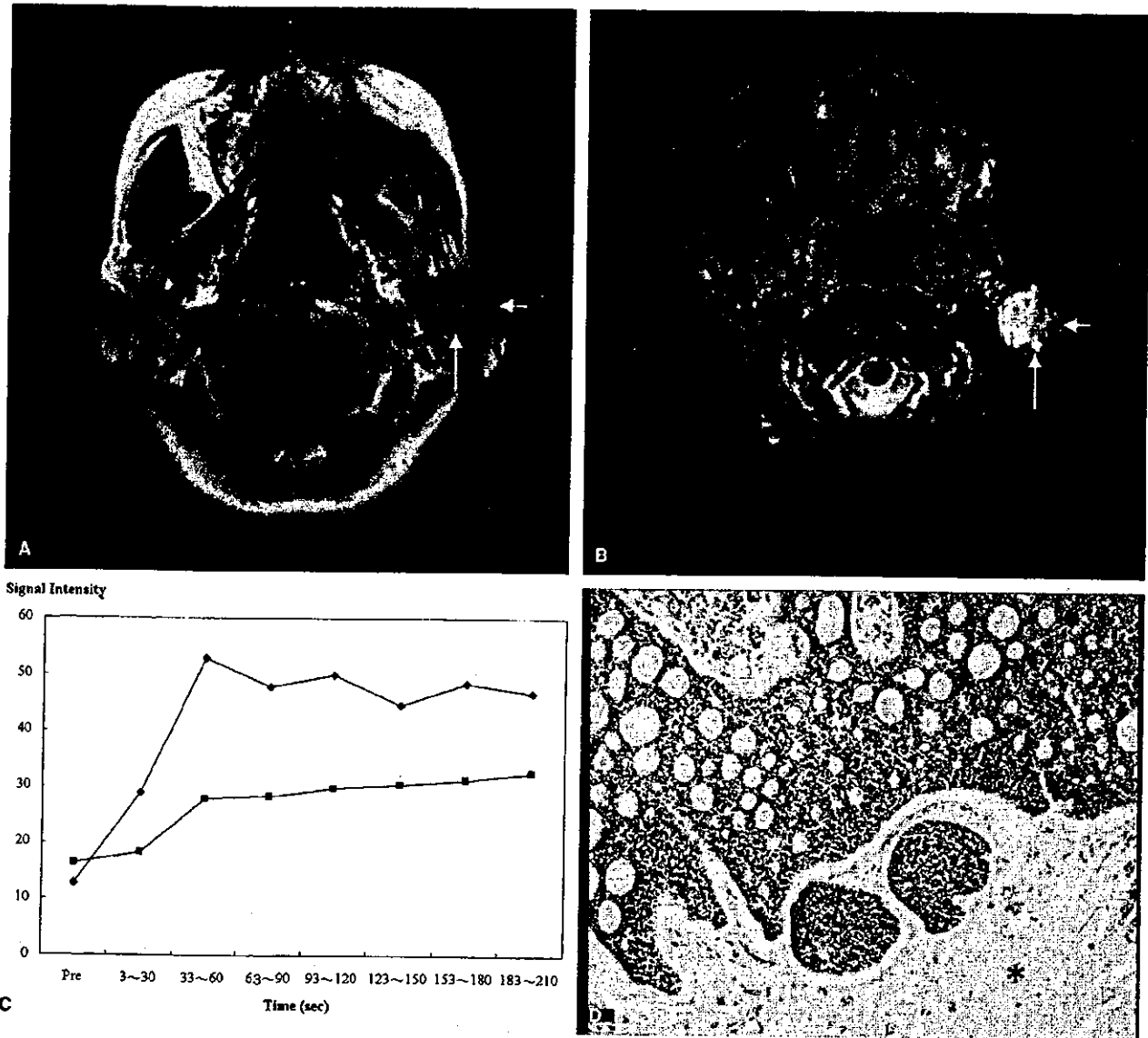
**FIGURE 10.** Adenoid cystic carcinoma in the left parotid gland of a 56-year-old woman. A, T1W image [400/9 (TR/TE), axial plane] of the maximal diameter section shows a lobulated tumor of isointensity (arrows). B, STIR (4000/30, axial plane) shows marked high-intensity tumor with ill-defined lateral border (arrows). C, The high-intensity region on STIR image has type D perfusion curve on dynamic MR images. The other region has type B perfusion curve. D, The region with marked high intensity on STIR images and type D perfusion curves on dynamic MR images is myxoid-rich tissue (*). The remaining region has nests of neoplastic epithelial cells containing several small, round, and pseudocystic structures.

showed type D curves, with a gradual upward slope, on dynamic MR images. On the other hand, the cellular tissue-predominant region of the time versus signal intensity curve peaked early. According to these results, our data agreed well with those of previous articles.[11–13] Abundant myxoid tissue with hypovascularity may account for the gradual increase in signal intensity, as Gd-DTPA may be distributed slowly and accumulate in the abundant extracellular matrix.

There were 4 malignant parotid tumors that showed type D curves. The region showing type D curves on dynamic MR images of adenoid cystic carcinoma had rich myxoid tissue and showed high intensity on STIR images. The other regions showing type D curves of salivary duct carcinoma had abundant fibrous stromata and necrotic foci, but did not show high intensity on STIR images. Thus, the myxoid component shows type D curves on dynamic images and high intensity on STIR images.
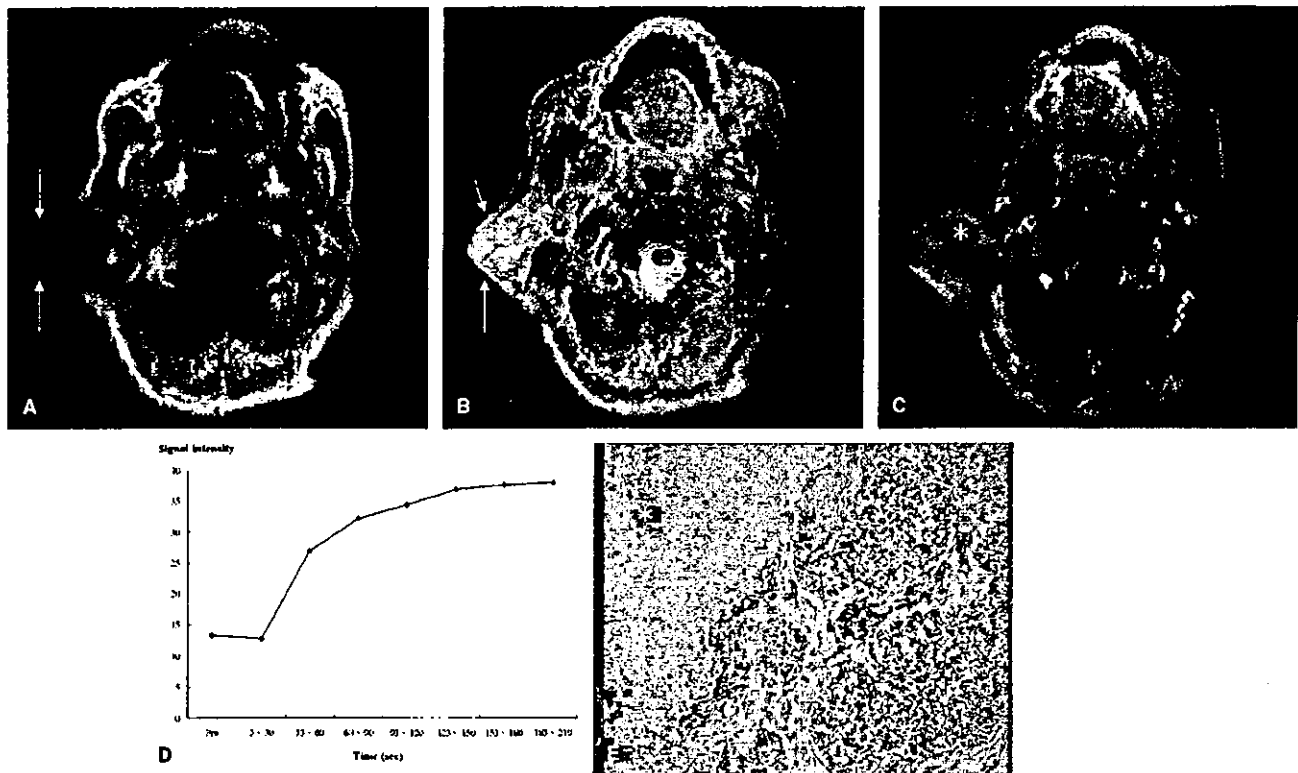
244

FIGURE 11. Salivary duct carcinoma in the right parotid gland of a 83-year-old man. A, T1W image [400/9 (TR/TE), axial plane] of the maximal diameter section shows a tumor with an ill-defined border of isointensity for muscle. The tumor invaded subcutaneous tissue (arrows). B, STIR (4000/30, axial plane) shows iso to moderate high-intensity tumor with subcutaneous invasion (arrows). C, On fat-suppression contrast-enhanced T1W images (400/20), the medial half of the tumor showed marked delay enhancement (*). The region had a high ADC value (1.79 × 10$^{-3}$ mm$^2$/s) on DW images, but had no characteristic high intensity on STIR images. D, All of the tumor at the same level as T1W and STIR images had type D perfusion curves on dynamic MR images. E, The pathologic specimen revealed small nets and cords of carcinomatous ductal epithelium within abundant fibrous tissue stroma and variably sized foci of necrosis (*).

Pleomorphic adenoma is composed of both epithelial and myxoid tissues. Myxoid components are also included in other tumors such as adenoid cystic carcinoma and neurogenic tumor. Our case of adenoid cystic carcinoma had an ill-defined margin that suggested invasive growth. Cellular-predominant regions with capillary vessels showed earlier maximal enhancement. Yabuuchi et al[13] reported that a short time of peak enhancement, less than 120 seconds, and a low WR of less than 30% on dynamic MR images, were useful criteria for the diagnosis of malignant tumor. According to our results, the WRs of all regions showing type A, B, or C perfusion curves on dynamic MR images were less than 30%, except a single region. Although there were some differences between the design of our dynamic study and that of theirs, they also experienced 2 cellular-predominant pleomorphic adenomas with high microvessel counts and less-cellularity stromata that could not be discriminated from malignant tumors on the basis of TIC type.

On DW images, the myxoid components showed high signal intensities. The calculated ADC values of the myxoid components were significantly higher than that of the spinal cord. The mean ADC value of the spinal cord, measured in the upper area of the neck in this study, was in good agreement with that previously reported.[14] The spinal cord has numerous nerve fibers with some cellularity and less extracellular space than myxoid tissues. These histopathological differences may generally explain the differences in the ADC values. Hypercellularity contributes to reducing the extracellular space and the diffusion space of water protons, with a resultant decrease in ADC values. The 2 different components of pleomorphic adenomas also reflected the differences in ADC values. Abundant myxoid areas showed high ADC values; on the other hand, the cellular areas consisting of numerous small cells and scanty myxoid stromata showed relatively low ADC values. According to Wang et al,[14] an ADC smaller than 1.22 × 10$^{-3}$ mm$^2$/s was one of the criteria to use for predicting malignancy.

In our study, all of the maximum and most of the minimum ADC values were higher than $1.22 \times 10^{-3}$ mm$^2$/s, but a few of the minimum ADC values were below $1.22 \times 10^{-3}$ mm$^2$/s. The average of the maximum ADC values of pleomorphic adenomas [2.03 ± 0.32 (SD), 1.47 to 2.51 × $10^{-3}$ mm$^2$/s) was higher ($P < 0.01$) than that of malignant tumors [1.40 ± 0.39 (SD), 0.80 to 2.10 × $10^{-3}$ mm$^2$/s]. The average of the minimum ADC values of pleomorphic adenomas [1.52 ± 0.30 (SD), 0.94 to 2.08 × $10^{-3}$ mm$^2$/s) was also higher ($P < 0.01$) than that of malignant tumors [1.01 ± 0.29 (SD), 0.48 to 1.35 × $10^{-3}$ mm$^2$/s].

MR findings of myxoid stroma, high intensity on STIR and T2W images, type D perfusion curves on dynamic MR images, and high ADC values on DW images have been considered as diagnostic clues for pleomorphic adenoma. In fact, there is a variety of MR findings of pleomorphic adenomas that reflects their cytomorphological and architectural variability. We speculated that hypercellularity with less-myxoid stroma reduced the intensity on STIR and T2W images and also reduced ADC values on DW images and resulted in an earlier TIC peak on dynamic MR images. These values and findings overlapped with those of malignant tumor. It stands to reason, then, that the variability of the MR findings of pleomorphic adenoma must be recognized and understood to avoid a misdiagnosis.

## CONCLUSIONS

There is great variability in the MR findings of pleomorphic adenoma, reflecting the various proportions of cellular and myxoid components. The diagnostic clue of pleomorphic adenoma is to find the myxoid component, which shows a high intensity on STIR and T2W images, progressive enhancement on dynamic MR images, and high ADC values on DW images. Hypercellularity with less-myxoid stroma reduced the intensity on STIR and T2W images and also reduced ADC values on DW images, bringing an earlier TIC peak on dynamic MR images. It is important to recognize that the MR images of hypercellularity with less-myxoid stroma could be overlapping with those of malignant parotid tumors. SIR$_{max}$ on STIR images and ADC values are significantly higher than those of malignant parotid tumors. Gradual enhancement curves on dynamic MR images without high intensity on STIR are shown in some malignant parotid tumors, reflecting abundant fibrosis. The combination findings— high intensity on STIR and T2W images, high ADC value on DW images, and type D perfusion curves on dynamic MR images—are useful for the detection of

myxoid tissue and predicting whether salivary gland tumors are benign or malignant.

## REFERENCES

1. Donovan DT, Conley JJ. Capsular significance in parotid tumor surgery: reality and myths of lateral lobectomy. *Laryngoscope.* 1984;94:324–329.
2. Dykun RJ, Deitel M, Borowy ZJ, et al. Treatment of parotid neoplasms. *Can J Surg.* 1980;23:14–19.
3. Myssiorek D, Ruah CB, Hybels RL. Recurrent pleomorphic adenomas of the parotid gland. *Head Neck.* 1990;12:332–336.
4. Touquet R, Mackenzie IJ, Carruth JA. Management of the parotid pleomorphic adenoma, the problem of exposing tumor tissue at operation. The logical pursuit of treatment policies. *Br J Oral Maxillofac Surg.* 1990;28:404–408.
5. Chaudhuri R, Bingham JB, Crossman JE, et al. Magnetic resonance imaging of the parotid gland using the STIR sequence. *Clin Otolaryngol.* 1992;17:211–217.
6. Schlakman BN, Yousem DM. MR of intraparotid masses. *AJNR Am J Neuroradiol.* 1993;14:1173–1180.
7. Tsushima Y, Matsumoto M, Endo K, et al. Characteristic bright signal of parotid pleomorphic adenomas on T2-weighted MR images with pathological correlation. *Clin Radiol.* 1994;49:485–489.
8. Joe VQ, Westesson PL. Tumors of the parotid gland: MR imaging characteristics of various histologic types. *AJR Am J Roentgenol.* 1994;163:433–438.
9. Ikeda K, Katoh T, Ha-Kawa SK, et al. The usefulness of MR in establishing the diagnosis of parotid pleomorphic adenoma. *AJNR Am J Neuroradiol.* 1996;17:555–559.
10. Mascaro L, Ferrari C, Grazioli L, et al. T2 relaxation of the parotid gland of patients affected by pleomorphic adenoma. *Magn Reson Imaging.* 1999;17:723–730.
11. Takashima S, Noguchi Y, Okumura T, et al. Dynamic MR imaging in the head and neck. *Radiology.* 1993;189:813–821.
12. Tsushima Y, Matsumoto M, Endo K. Parotid and parapharyngeal tumors: tissue characterization with dynamic magnetic resonance imaging. *Br J Radiol.* 1994;67:342–345.
13. Yabuuchi H, Fukuya T, Tajima T, et al. Salivary gland tumors: diagnostic value of gadolinium-enhanced dynamic MR imaging with histopathologic correlation. *Radiology.* 2003;226:345–354.
14. Wang J, Takashima S, Takayama F, et al. Head and neck lesions: characterization with diffusion-weighted echo-planar MR imaging. *Radiology.* 2001;220:621–630.
15. Vogl TJ, Dresel SH, Spath M, et al. Parotid gland: plain and gadolinium-enhanced MR imaging. *Radiology.* 1990;177:667–674.
16. Freling NJ, Molenaar WM, Vermey A, et al. Malignant parotid tumors: clinical use of MR imaging and histologic correlation. *Radiology.* 1992;185:691–696.
17. Browne RF, Golding SJ, Watt-Smith SR. The role of MRI in facial swelling due to presumed salivary gland disease. *Br J Radiol.* 2001;74:127–133.
18. Hee CG, Perry CF. Fine-needle aspiration cytology of parotid tumours: is it useful? *Aust N Z J Surg.* 2001;71:345–348.
19. Zbaren P, Schar C, Hotz MA, et al. Value of fine-needle aspiration cytology of parotid gland masses. *Laryngoscope.* 2001;111:1989–1992.
20. Eveson JW, Cawson RA. Salivary gland tumours. A review of 2410 cases with particular reference to histological types, site, age and sex distribution. *J Pathol.* 1985;146:51–58.
21. Chaudhuri R, Cleeson MJ, Graves PE, et al. MR evaluation of the parotid gland using STIR and gadolinium-enhanced imaging. *Eur Radiol.* 1992;2:357–364.

# Selective Intra-Arterial 3-Dimensional Computed Tomography Angiography for Preoperative Evaluation of Nephron-Sparing Surgery

*Takuya Ueda, MD,* * *Toyofusa Tobe, MD,† Seiji Yamamoto, MD,‡ Ken Motoori, MD,‡*
*Yoshitaka Murakami, PhD,§ Tatsuo Igarashi, MD,‖ and Hisao Ito, MD* *

**Objective:** To evaluate selective intra-arterial 3-dimensional computed tomography (3D-CT) angiography as a tool for the preoperative evaluation of nephron-sparing surgery (NSS).

**Methods:** Twenty-three patients with renal cell carcinoma indicating NSS underwent selective intrarenal 3D-CT angiography. The time-lapse dual-phase technique was used for simultaneous vascular and urographic visualization. The 3D images were created by the shaded volume-rendering method. The CT attenuation of target structures was measured for quantitative evaluation. The 3D images were visually evaluated for the renal artery, vein, and collecting system using a grading system. Results were statistically analyzed.

**Results:** The 3D-CT angiography depicted the intrarenal branches of the renal artery and vein and the whole collecting system in most patients. Visualization of the renal artery was significantly correlated to its CT attenuation. Visualization of the renal vein was correlated to its CT attenuation adjusted by the surrounding renal parenchyma.

**Conclusion:** Selective intra-arterial 3D-CT angiography allows the detailed visualization of intrarenal structures.

**Key Words:** computed tomography (CT), three-dimensional, carcinoma, renal cell, nephron-sparing surgery

*(J Comput Assist Tomogr 2004;28:496–504)*

M otivated by several trends, including advances in renal imaging and improved surgical management, nephron-sparing surgery (NSS) has become an established optional treatment of renal cell carcinoma (RCC).[1,2] The accumulation of data has provided evidence of the long-term functional advantage gained by the maximal preservation of unaffected renal parenchyma using NSS, without sacrificing cancer control and patient satisfaction.[1-8]

Acceptable indications for NSS may be divided into 2 categories: imperative and elective indications. Imperative indications include RCC involving an anatomically or functionally solitary kidney caused by unilateral renal agenesis, previous contralateral nephrectomy, or irreversible impairment of contralateral renal function because of a benign disorder.[2,9,10] Patients with bilateral synchronous RCC also have an imperative indication.[11] Nephron-sparing surgery should also be attempted for patients in whom the contralateral kidney is threatened by local, systemic, or genetic conditions that may affect future function or for patients with the likelihood of subsequent contralateral tumors.[2] Elective indications include small, localized, often incidental RCC with a normal contralateral kidney.[1,2,7] Although patient selection for elective indications is still controversial, recent studies have indicated a significantly lower rate of recurrence and significantly improved length of survival after NSS for tumors 4 cm or less in diameter.[1,2,12,13]

Nephron-sparing surgery is technically more challenging than open nephrectomy.[2,6,14] Different from the en bloc removal of the kidney with tumor in open nephrectomy, NSS requires management of intrarenal structures, including intrarenal segments of the renal artery and vein as well as the collecting system.[1-15] Tumor excision is performed by wedge or segmental resection, also obtaining a thin margin of adjacent normal parenchyma.[2,6,14] Incomplete resection of the primary tumor leads to local recurrence.[1-3] Temporary vascular occlusion is performed during the procedure to decrease bleeding and renal tissue turgor,[2,15] and minimizing the duration of vascular occlusion reduces the risk of renal ischemic injury and the need for subsequent hemodialysis.[8,15] Watertight closure of the collecting system is required, when encountered, to prevent urinary fistula formation.[2,16] Removal of a centrally located tumor is technically more demanding than removal of a peripheral one.[17,18] To prevent transection of major branches

of the renal artery and vein, any significant intrarenal branches must be identified.[17,18] Imperative indications constrain the compulsory execution of NSS in such a technically difficult condition, because the alternative would yield the patient anephric if a nephrectomy is performed.[2,8]

Preoperative imaging for open nephrectomy has been used to assess tumor size, extent, invasion, distant and/or lymph node metastasis, and relevant vascular anatomy.[2,19] The technical difficulty of NSS requires more detailed anatomic information. Preoperative information concerning the vascular anatomy and collecting system and their relation to the tumor contributes to early vascular control, avoidance of renal ischemia, complete tumor excision with negative margins, precise closure of the collecting system, careful hemostasis, and closure of the renal defect.[2,13,14] The higher risk in removal of a centrally located tumor demands more detailed preoperative assessment of intrarenal structures.[16-18]

Many reports have emphasized the usefulness of intravenous 3-dimensional computed tomography (3D-CT) angiography for NSS, integrating essential information from angiography, venography, excretory urography, and conventional 2-dimensional CT into a single preoperative staging test.[20-26] The intravenous technique has limits in terms of depicting peripheral branches of renal arteries and veins, collecting systems, and their interrelations to the tumor, however.[27-29] Recently, advances in multidetector-row CT technology and the 3D processing workstation have led to more frequent clinical applications of high-performance 3D imaging.[30] Some reports have described the enhanced ability of 3D visualization with the intra-arterial CT acquisition technique for several organs.[31,32]

We performed selective intra-arterial volume-rendered 3D-CT angiography using multidetector-row CT in patients with NSS-indicated RCC. The purpose of this article is to assess selective intra-arterial 3D-CT angiography as a tool for the preoperative evaluation of NSS, emphasizing its visualization of the renal artery and vein as well as the collecting system. Indications for the application of this method are also discussed.

## MATERIALS AND METHODS

### Subjects

A total of 23 patients (19 men and 4 women) were prospectively examined between September 2000 and August 2003. Thirteen patients had been referred from other hospitals for determination of the indications for NSS; NSS was contraindicated in 11 of these patients because of technical difficulties at these hospitals (6 had centrally located tumors and 5 had renal hilar tumors). Seven patients had been followed for urologic disease and 3 for nonurologic disease at our hospital. All patients were diagnosed with RCC by preceding CT or ultrasound examination and were considered to have possible indi-

cations for NSS at our hospital. The mean age of these patients was 63.4 years (range: 40–78 years), and their mean weight was 57.5 kg (range: 43–76 kg). In accordance with our institutional review board guidelines, written informed consent was obtained from all patients before their inclusion in the study. Among all 23 patients, the indications for surgery were elective in 15 and imperative in 8. The imperative indications in these 8 patients were a solitary kidney because of a previous history of bilateral asynchronous tumors in 4, bilateral synchronous tumors in 2, and a functional solitary kidney with contralateral renal atrophy because of chronic urolithiasis in 2.

### Data Acquisition Technique

Selective renal arteriography and intra-arterial CT angiography were performed using combined digital subtraction angiography and a multidetector-row CT system (Infinix ACTIV/Aquilion; Toshiba Medical Systems, Tokyo, Japan). The angiographic procedure was performed by means of a transfemoral approach and the Seldinger technique using a standard diagnostic catheter. Selective renal arteriography was obtained using 12 mL contrast material (Iohexol, Omnipaque 300; Daiichi Pharmaceutical, Tokyo, Japan) at a rate of 3 mL/s. After the renal arteriography, the digital subtraction angiography unit was switched to the CT mode. Nonenhanced CT was performed to determine the scanning range for CT angiography. After nephrographic enhancement was confirmed with digital subtraction angiography by means of a preceding infusion of contrast medium, CT acquisition was performed 5 seconds after the beginning of a bolus infusion of 40 mL 50% diluted contrast material at a rate of 2 mL/s. Scanning parameters were set at a tube current of 300 mAs, a voltage of 120 kV, a scan time of 0.5 seconds per rotation, and a 1.0-mm slice thickness with a helical pitch of 5. The scanning range was between 150 and 200 mm depending on the patient, with total scanning time being between 15 and 20 seconds.

After the CT examination, DSA aortography was performed to identify the presence of multiple renal arteries. If multiple renal arteries were confirmed, additional renal arteriography was performed for all accessory renal arteries on the side with the tumor. Additional intra-arterial CT angiography was planned for any case with an accessory renal artery with arterial perfusion for the tumor, but there was no such case in the present series.

### Quantitative Measurement of Enhancement

Quantitative measurements were performed by a single radiologist (T.U.). To evaluate enhancement of the target structures and surrounding renal cortex and medulla, the Hounsfield unit (HU) number on 2-dimensional images was measured to set regions of interest for the renal artery, vein, calyx, renal cortex, and medulla.

## Three-Dimensional Data Processing

Volume data of CT acquisition were reconstructed at 1.0-mm intervals, with 150- to 180-mm region of interests with 512 × 512 matrices. Reconstructed images were transferred to a commercial workstation for 3D processing (Virtual Place M, Medical Imaging Laboratory and Office Azemoto, Tokyo, Japan).

The radiologist (T.U.) created all the 3D images by means of the volume-rendering method. A linear ramp-shaped opacity curve was used for the transfer function of the volume-rendering parameters. Optimized parameters in each patient were determined visually using the following procedures. First, CT attenuations corresponding to 0% and 100% opacities were set to 0 and 1000 HU, respectively. The volume data were then sectioned through the longitudinal axis of the kidney to visualize the inner structures. Finally, lower and upper cut-off values corresponding to 0% and 100% attenuation were adjusted so that intrarenal branches of the renal artery and the renal vein and urinary tract were the most visible.

The 3D volume-rendered images were created as a movie file (formatted as an audio visual, and still images [AVI] file) continuously scrolling the cut planes, where the view point was set from the posterior lateral view and the cut planes were set parallel to the longitudinal axis of the kidney.

## Visual Evaluation of 3-Dimensional Images

Two radiologists (K.M. and S.Y., with 10 and 11 years of experience in abdominal radiology, respectively) independently evaluated the movies of the 3D images without knowledge of any clinical information. They evaluated the 3D image movies by means of the cine loop mode, and they freely stilled any 3D image for static evaluation if deemed necessary.

The movies of the 3D images were visually scored using a grading system. Scores were assigned to each structure, including the renal artery, vein, and urinary tract. Visualization of the renal artery and vein was scored as follows: 5, fifth-order branches were visualized; 4, fourth-order branches were visualized; 3, third-order branches were visualized; 2, second-order branches were visualized; and 1, main branches or none were visualized (Figs. 1, 2). Visualization of the urinary tract was scored as follows: 4, minor calyces were visualized; 3, major calyces were visualized; 2, renal pelvis was visualized; and 1, poor visualization of the collecting system (Fig. 3). The best-visualized segments were scored for variance of visualization at each evaluation.

For the detectability of intrarenal segments of the renal artery, the number of second-order branches of the renal artery was recorded. Selective renal arteriography was used as the gold standard.

## Statistical Analyses

Statistical analysis methods were designed and performed by a single statistician (Y.M.). One-way analysis of variance (ANOVA) was used for comparisons between visual evaluation and clinical status, including age, sex, indication, TNM classification, tumor location, and renal function.

To assess interobserver agreement for the visual evaluation of each structure, the κ value was calculated (for the κ value, <0.20 was considered to indicate poor agreement; 0.21–0.40, fair agreement; 0.41–0.60, moderate agreement; 0.61–0.80, good agreement; and 0.81–1.00, excellent agreement).

To assess the correlation between visual evaluation and CT attenuation, patients were grouped by the grade of each visual evaluation of the renal artery, vein, and urinary tract. To compare CT attenuation between groups of visual evaluation, one-way ANOVA was used for analysis. To adjust the effects of the renal cortex and medulla to each visual evaluation of the renal artery, vein, and urinary tract, each covariate of the renal artery, vein, and calyx was added to the analysis of covariance (ANCOVA).

For all statistical analyses, differences were considered to be statistically significant at $P < 0.05$.

## Review of Surgical Result

Preoperative planning was discussed by a single radiologist (T.U.) and a single urologist (T.T.). Intraoperative surgical findings were reviewed to determine any findings unexpected by the preoperative evaluation of 3D images. Postoperative complications were also reviewed.
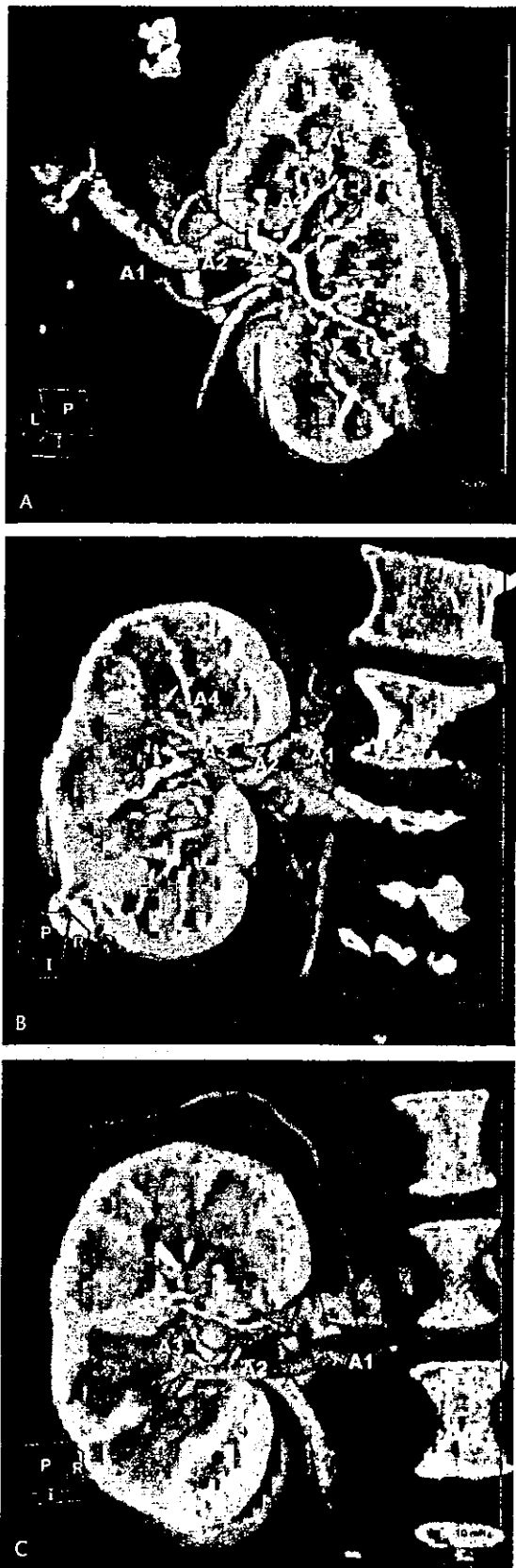
## RESULTS

All examinations were successfully performed according to our protocol without complications. The mean time for the entire angiographic procedure was about 45 minutes (range: 30–63 minutes). The times for 3D processing and visual evaluation of 3D images were about 10–15 minutes and 10–20 minutes, respectively, for each patient.

Digital subtraction angiography aortography demonstrated a single renal artery in 17 patients and double renal arteries in 6 patients. Among the latter 6 patients, 1 had an accessory branch on the ipsilateral side with tumor, 2 had renal arteries bilaterally, and 3 had a renal artery on the contralateral side. Selective renal arteriography was performed for the accessory branch on the side with tumor. None of these patients showed arterial perfusion to the tumor. In the patients with double renal arteries, intra-arterial 3D-CT angiography demonstrated a lack of contrast enhancement in the area corresponding to arterial perfusion of the accessory branch. In 2 patients, double renal veins were detected on the side with tumor by intra-arterial 3D-CT angiography.

## Results of Visual Evaluation

The results of the visual evaluation are shown in Table 1. There was excellent agreement between the observers regarding the renal artery, vein, and urinary tract (κ values were 0.824, 0.904, and 0.839, respectively). There was no signifi-

cant difference between visual evaluation and clinical status of age, sex, indication, TNM classification, and tumor location. Only renal function was correlated with visualization of the collecting system with statistical significance ($P < 0.01$).

The renal artery was shown with fourth-order or higher peripheral branches in 22 patients (see Figs. 1A, B), and only third-order branches were visualized in 1 patient (see Fig. 1C). The renal vein was revealed with third-order or higher peripheral branches in 22 patients (see Figs. 2A–C), and only second-order branches were visualized in 1 patient (see Fig. 2D), in whom the renal vein and renal parenchyma showed enhancement with almost the same CT attenuation. Urinary tracts as far as minor calyces were clearly visualized in 21 patients (see Figs. 3A, B). In contrast, only renal pelvises were visualized in 2 patients. They showed mild hydronephrosis, and their collecting systems were poorly enhanced (see Fig. 3C).

Of 83 second-order branches of the renal artery identified by selective renal arteriography, 80 were detected by 3D images (96.4%). The 3 missed branches were retrospectively reviewed. One was identified in retrospect, 1 was identified on the source 2-dimensional image showing nonhomogeneous enhancement by lamina flow, and 1 was not identified for unknown reasons.

## Correlation Between Quantitative Measurement and Visual Evaluation

Table 2 shows mean CT attenuation grouped according to the grades of each visual evaluation. One-way ANOVA revealed a statistically significant difference in CT attenuation of the renal artery between the grades ($P < 0.001$) but no statistically significant difference in CT attenuation of the renal vein and renal calyx.

Analysis of covariance with controlled effects of the renal cortex and medulla revealed statistically significant differences in CT attenuation of the renal vein ($P = 0.01$ and $P = 0.02$, respectively) but no statistically significant difference in CT attenuation of the renal artery and calyx.

## Surgical Results

Among the 15 patients with an elective indication, 7 underwent NSS, 5 underwent open nephrectomy, and 3 underwent laparoscopic nephrectomy, all performed on the basis of the patients' own informed decisions. All 8 patients with an imperative indication underwent NSS. In total, 13 patients underwent NSS, all of whom were proven to have RCC histopathologically.

FIGURE 1. Selective intra-arterial volume-rendered 3-dimensional computed tomography angiographic images demonstrated different visualization scores for the peripheral renal arteries in 3 patients: score of 5 (A), score of 4 (B), and score of 3 (C). The numbers in the figures (A1–A5) show the order of the renal arterial branches.
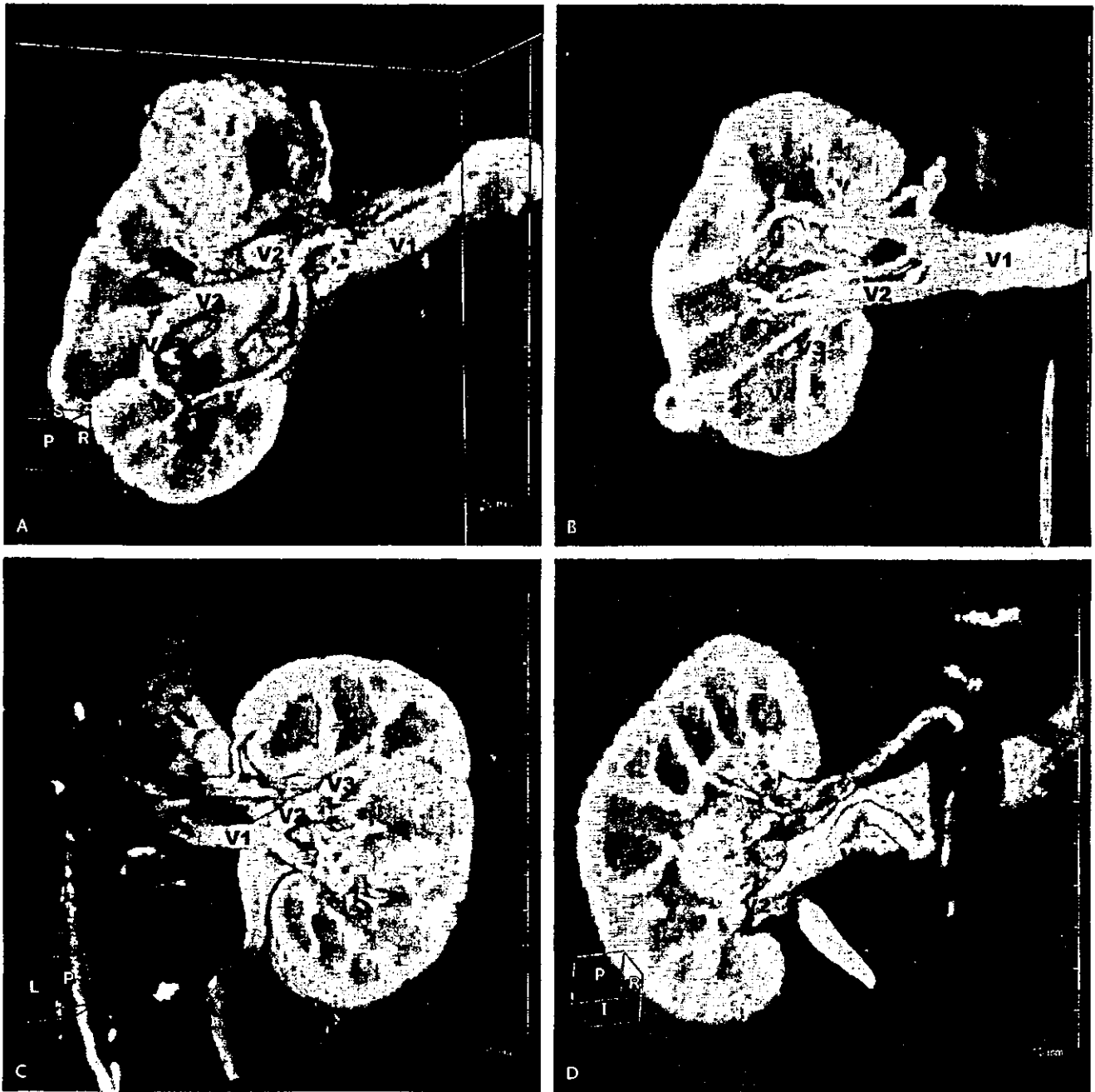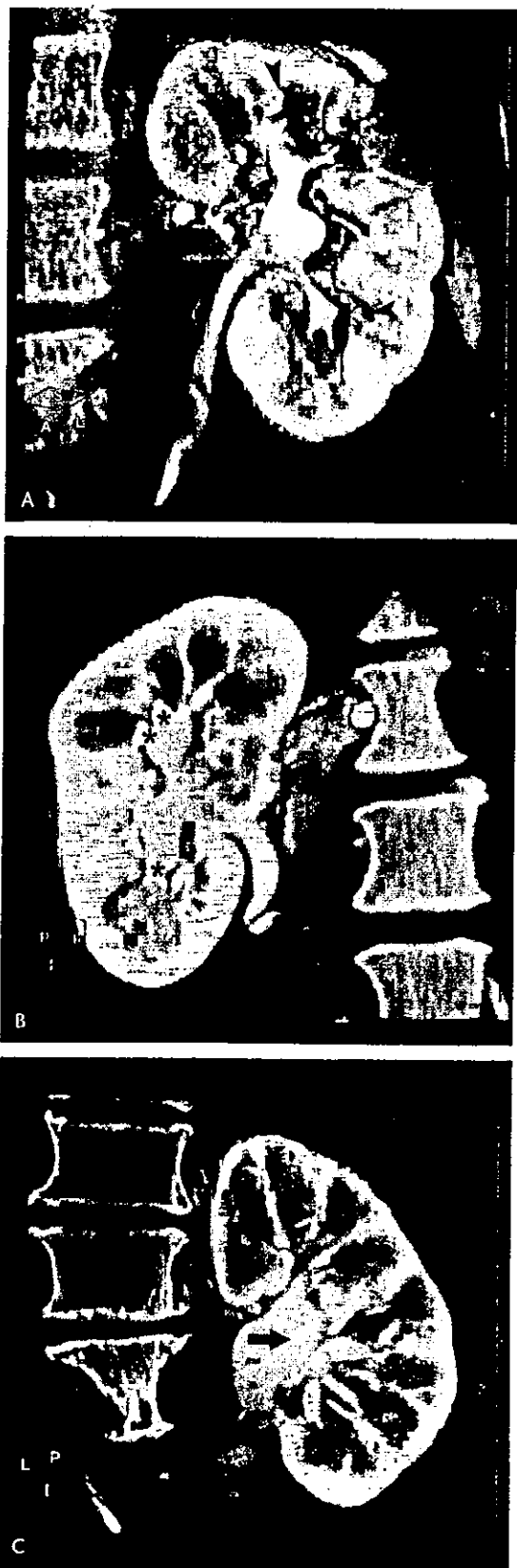
**FIGURE 2.** Selective intra-arterial volume-rendered 3-dimensional computed tomography angiographic images demonstrated different visualization scores for the peripheral renal veins in 4 patients: score of 5 (A), score of 4 (B), score of 3 (C), and score of 2 (D). The numbers in the figures (V1–V5) show the order of the renal venous branches. C, Double renal veins were detected (arrows).

In 1 patient, a dilated capsular artery was detected during surgery that had been undetected on selective renal arteriography and intra-arterial 3D-CD angiography. Unexpected arterial bleeding occurred in 1 patient at wedge resection in spite of vascular occlusion. This might have resulted from an acces- sory renal artery missed by preoperative evaluation but was not confirmed, because hemostasis was performed at peripheral arterial segments in the surgical plane.

Postoperative complications were observed in 4 pa- tients. Bleeding and continuous hematoma occurred in 1 pa-

tient, and an additional open nephrectomy was performed. Transient renal failure occurred in 1 patient, with recovery being achieved by means of temporal hemodialysis. Transient renal malfunction occurred in 2 patients, and this was recovered only with conservative therapy.

## DISCUSSION

Nephron-sparing surgery requires detailed preoperative information concerning the vascular anatomy and collecting system and their relation to the tumor. Many reports have provided evidence of the usefulness of 3D volume-rendered CT angiography for preoperative imaging of NSS.[20–26] Nevertheless, their intravenous techniques had some limitations in terms of 3D visualization of the intrarenal structures.[20–29] The detectability of vascular structures has allowed arterial branches to be recognized at the segmental level and venous branches at the submain level. Basically, intrarenal branches are hard to visualize.[27–29] Few have discussed the depiction of the urinary collecting system during 3D-CT angiography, whereas there have been many reports about the usefulness of intravenous CT urography.[33] Because CT urography is obtained in the excretory phase, vascular structures and the collecting system must be evaluated with separate images in the different phases.

We performed volume-rendering 3D-CT angiography with an intra-arterial bolus infusion of contrast medium. A time-lapse dual-phase infusion of contrast medium was used in combination. Our method has some advantages compared with previously reported intravenous 3D-CT angiography.

Basically, volume-rendering 3D image segments structures on the basis of voxel attenuation. Therefore, the quality of the 3D image is empirically dependent on the contrast of CT attenuation between the target structures and surrounding tissues.[34,35] The intra-arterial infusion technique achieves higher contrast resolution in each structure than the intravenous technique.[31,32] Therefore, our intra-arterial technique achieved a detailed depiction of the intrarenal branches of renal arteries and veins; fourth-order branches of the renal artery and third-order branches of the renal vein were visualized in most cases.

The time-lapse dual-phase technique results in satisfactory urographic opacification of the collecting system while maintaining high opacification of vascular structures. This integrated the preoperative information for visualizing the vascular structures and collecting system simultaneously on a 3D image.

**FIGURE 3.** Selective intra-arterial volume-rendered 3-dimensional computed tomography angiographic images demonstrated different visualization scores for the urinary tract in 3 patients: score of 4, minor calyces (arrowheads) were visualized (A); score of 3, major calyces (asterisks) were visualized (B); and score of 2, renal pelvis (arrow) was visualized (C).

**TABLE 1.** Summary of Visual Evaluation for Each Renal Structure

| Patient No. | Renal Artery | | Renal Vein | | Urinary Tract | |
|---|---|---|---|---|---|---|
| | Observer 1 | Observer 2 | Observer 1 | Observer 2 | Observer 1 | Observer 2 |
| 1 | 5 | 5 | 5 | 5 | 4 | 4 |
| 2 | 5 | 5 | 3 | 3 | 4 | 4 |
| 3 | 5 | 4 | 3 | 3 | 4 | 4 |
| 4 | 4 | 4 | 3 | 3 | 4 | 4 |
| 5 | 5 | 5 | 3 | 3 | 4 | 4 |
| 6 | 3 | 3 | 2 | 2 | 2 | 2 |
| 7 | 5 | 5 | 4 | 4 | 4 | 4 |
| 8 | 4 | 4 | 3 | 3 | 4 | 4 |
| 9 | 5 | 5 | 4 | 4 | 4 | 4 |
| 10 | 5 | 5 | 4 | 4 | 4 | 4 |
| 11 | 4 | 4 | 4 | 3 | 4 | 4 |
| 12 | 5 | 5 | 3 | 3 | 2 | 2 |
| 13 | 5 | 5 | 3 | 3 | 4 | 4 |
| 14 | 5 | 5 | 3 | 3 | 3 | 3 |
| 15 | 4 | 4 | 3 | 3 | 4 | 4 |
| 16 | 4 | 4 | 3 | 3 | 3 | 4 |
| 17 | 5 | 5 | 3 | 3 | 4 | 4 |
| 18 | 5 | 5 | 5 | 5 | 4 | 4 |
| 19 | 4 | 4 | 3 | 3 | 4 | 4 |
| 20 | 4 | 4 | 3 | 3 | 4 | 4 |
| 21 | 5 | 5 | 3 | 3 | 4 | 4 |
| 22 | 5 | 5 | 3 | 3 | 4 | 4 |
| 23 | 4 | 4 | 3 | 3 | 4 | 4 |
| Mean | 4.565 | 4.522 | 3.304 | 3.261 | 3.739 | 3.783 |
| ±SD | ±0.590 | ±0.593 | ±0.703 | ±0.689 | ±0.619 | ±0.600 |

Data are visualization scores.

In our method, only a 10-minute period is required for 3D data processing, which is quite acceptable for clinical use.

The major disadvantage of this procedure is the invasiveness of the intra-arterial technique. A less invasive technique would be preferable for the preoperative examination. Although there was no significant difference in outcome in patients treated with NSS for centrally and peripherally located tumors, removal of tumors from a central and/or hilar location is technically more demanding.[2,17,18] This technical difficulty might reduce the chance of an indication for NSS in some patients. In fact, 11 patients indicated for NSS in our hospital were first contraindicated in other institutions, although this difference might be ascribed not only to the issue of preoperative evaluation but to the practical issue of surgery. Detailed evaluation may salvage some operable patients who might otherwise be contraindicated for NSS because of the technical difficulty of the procedure; these patients might become anephric if a nephrectomy is performed and require chronic hemodialy-

sis. Therefore, our invasive method confers a benefit to patients with large and/or centrally located tumors, especially to those judged with imperative indications.

Expected complications of this procedure may include hemorrhage, infection, and thromboembolism, although no patients in the present series incurred any such major complications. Radiation exposure by means of intra-arterial 3D-CT angiography is the same as by the intravenous technique. A potential pitfall of our method is the possibility of missing accessory branches of multiple renal arteries because of its selective procedure. Aortography needs to be checked carefully. Any cortical defect of contrast enhancement in 3D-CT angiography may be a clue concerning the presence of accessory branches.

A limitation of this study was the small number of patients. Further evaluations with larger patient populations are required to establish clinical implications and indications. The visualization of this method should also be compared with that

**TABLE 2.** CT Attenuation of Each Structure Grouped by Its Visualization Scores

| Score | CT Attenuation Grouped by Score of Renal Artery | | | CT Attenuation Grouped by Score of Renal Vein | | | CT Attenuation Grouped by Score of Urinary Tract | | |
|---|---|---|---|---|---|---|---|---|---|
| | Renal Artery | Cortex | Medulla | Renal Vein | Cortex | Medulla | Urinary Tract | Cortex | Medulla |
| 5 | 765.1 ± 109.6 (14) | 555.2 ± 113.3 (14) | 153.6 ± 53.4 (14) | 542.5 ± 135.1 (2) | 519.0 ± 111.7 (2) | 113.0 ± 117.4 (2) | | | |
| 4 | 510.9 ± 66.9 (8) | 480.0 ± 91.7 (8) | 161.5 ± 58.0 (8) | 602.0 ± 144.7 (4) | 610.0 ± 156.7 (4) | 165.0 ± 16.1 (4) | 1159 ± 550.7 (19) | 520.0 ± 116.4 (19) | 154.1 ± 54.3 (19) |
| 3 | 350.0 ± 0.0 (1) | 600.0 ± 0.0 (1) | 220.0 ± 0.0 (1) | 536.6 ± 132.7 (16) | 508.4 ± 95.0 (16) | 159.8 ± 53.0 (16) | 1004 ± 291.3 (2) | 562.5 ± 23.3 (2) | 149.5 ± 64.3 (2) |
| 2 | / (0) | / (0) | / (0) | 288.0 ± 0.0 (1) | 600.0 ± 0.0 (1) | 220.0 ± 0.0 (1) | 200.0 ± 14.1 (2) | 604.5 ± 6.36 (2) | 218.0 ± 2.82 (2) |
| 1 | / (0) | / (0) | / (0) | / (0) | / (0) | / (0) | / (0) | / (0) | / (0) |

Data are mean ± SD of CT attenuation (HU). Numbers in parentheses indicate the number of patients.
/, no data.

of other modalities, especially with intravenous 3D-CT angiography. Another limitation of this technique is the as yet limited availability of the combined angiography and multidetector-row CT system, although some reports have emphasized the usefulness of the combined system for several organs and that this system is commercially available.[31,32]

In conclusion, we performed selective intra-arterial 3D-CT angiography for the preoperative evaluation of NSS. This method integrates detailed intrarenal anatomic information regarding the renal artery, vein, and urinary collecting system. Although further evaluation is required to establish its clinical application, the ability to visualize intrarenal structures may be helpful for the technically difficult NSS, especially for the cases with an imperative indication.

## ACKNOWLEDGMENTS

## REFERENCES

1. Filipas D, Fichtner J, Spix C, et al. Nephron-sparing surgery of renal cell carcinoma with a normal opposite kidney: long-term outcome in 180 patients. *Urology*. 2000;56:387–392.
2. Uzzo RG, Novick AC. Nephron sparing surgery for renal tumors: indications, techniques and outcomes. *J Urol*. 2001;166:6–18.
3. Hafez KS, Fergany AF, Novick AC. Nephron sparing surgery for localized renal cell carcinoma: impact of tumor size on patient survival, tumor recurrence and TNM staging. *J Urol*. 1999;162:1930–1933.
4. Fergany AF, Hafez KS, Novick AC. Long-term results of nephron sparing surgery for localized renal cell carcinoma: 10-year followup. *J Urol*. 2000;163:442–445.
5. Shinohara N, Harabayashi T, Sato S, et al. Impact of nephron-sparing surgery on quality of life in patients with localized renal cell carcinoma. *Eur Urol*. 2001;39:114–119.
6. Delakas D, Karyotis I, Daskalopoulos G, et al. Nephron-sparing surgery for localized renal cell carcinoma with a normal contralateral kidney: a European three-center experience. *Urology*. 2002;60:998–1002.
7. Matin SF, Gill IS, Worley S, et al. Outcome of laparoscopic radical and open partial nephrectomy for the sporadic 4 cm or less renal tumor with a normal contralateral kidney. *J Urol*. 2002;168:1356–1360.
8. Shekarriz B, Upadhyay J, Shekarriz H, et al. Comparison of costs and complications of radical and partial nephrectomy for treatment of localized renal cell carcinoma. *Urology*. 2002;59:211–215.
9. Ghavamian R, Cheville JC, Lohse CM, et al. Renal cell carcinoma in the solitary kidney: an analysis of complications and outcome after nephron sparing surgery. *J Urol*. 2002;168:454–459.
10. Gacci M, Rizzo M, Lapini A, et al. Imperative indications for conservative surgery for renal cell carcinoma: 20 years' experience. *Urol Int*. 2001;67:203–208.
11. Baltaci S, Orhan D, Soyupek S, et al. Influence of tumor stage, size, grade, vascular involvement, histological cell type and histological pattern on multifocality of renal cell carcinoma. *J Urol*. 2000;164:36–39.
12. Schlichter A, Wunderlich H, Junker K, et al. Where are the limits of elective nephron-sparing surgery in renal cell carcinoma? *Eur Urol*. 2000;37:517–520.
13. Butler BP, Novick AC, Miller DP, et al. Management of small unilateral renal cell carcinomas: radical versus nephron-sparing surgery. *Urology*. 1995;45:34–41.
14. Ghavamian R, Zincke H. Open surgical partial nephrectomy. *Semin Urol Oncol*. 2001;19:103–113.
15. Mejean A, Vogt B, Cazin S, et al. Nephron sparing surgery for renal cell carcinoma using selective renal parenchymal clamping. *J Urol*. 2002;167:234–235.
16. Uzzo RG, Cherullo EE, Myles J, et al. Renal cell carcinoma invading the urinary collecting system: implications for staging. *J Urol*. 2002;167:2392–2396.
17. Hafez KS, Novick AC, Butler BP. Management of small solitary unilateral renal cell carcinomas: impact of central versus peripheral tumor location. *J Urol*. 1998;159:1156–1160.
18. Chan DY, Marshall FF. Partial nephrectomy for centrally located tumors. *Urology*. 1999;54:1088–1092.
19. Sheth S, Scatarige JC, Horton KM, et al. Current concepts in the diagnosis and management of renal cell carcinoma: role of multidetector CT and three-dimensional CT. *Radiographics*. 2001;21(Spec No):S237–S254.
20. Smith PA, Marshall FF, Corl FM, et al. Planning nephron-sparing renal surgery using 3D helical CT angiography. *J Comput Assist Tomogr*. 1999;23:649–654.

21. Coll DM, Uzzo RG, Herts BR, et al. Three-dimensional volume rendered computerized tomography for preoperative evaluation and intraoperative treatment of patients undergoing nephron sparing surgery. *J Urol.* 1999; 161:1097–1102.

22. Wunderlich H, Reichelt O, Schubert R, et al. Preoperative simulation of partial nephrectomy with three-dimensional computed tomography. *BJU Int.* 2000;86:777–781.

23. Coll DM, Herts BR, Davros WJ, et al. Preoperative use of 3D volume rendering to demonstrate renal tumors and renal anatomy. *Radiographics.* 2000;20:431–438.

24. Remer EM, Herts BR, Veniero JC. Imaging for nephron-sparing surgery. *Semin Urol Oncol.* 2002;20:180–191.

25. Marukawa K, Horiguchi J, Shigeta M, et al. Three-dimensional navigator for retroperitoneal laparoscopic nephrectomy using multidetector row computerized tomography. *J Urol.* 2002;168:1933–1936.

26. Derweesh IH, Herts B, Novick AC. Three-dimensional image reconstruction for preplanning of renal surgery. *Urol Clin North Am.* 2003;30:515–528.

27. Platt JF, Ellis JH, Korobkin M, et al. Helical CT evaluation of potential kidney donors: findings in 154 subjects. *AJR Am J Roentgenol.* 1997;169: 1325–1330.

28. Urban BA, Ratner LE, Fishman EK. Three-dimensional volume-rendered CT angiography of the renal arteries and veins: normal anatomy, variants, and clinical applications. *Radiographics.* 2001;21:373–386.

29. Pannu HK, Fishman EK. Multidetector computed tomographic evaluation of the renal artery. *Abdom Imaging.* 2002;27:611–619.

30. Calhoun PS, Kuszyk BS, Heath DG, et al. Three-dimensional volume rendering of spiral CT data: theory and method. *Radiographics.* 1999;19: 745–764.

31. Hirai T, Korogi Y, Ono K, et al. Preoperative evaluation of intracranial aneurysms: usefulness of intraarterial 3D CT angiography and conventional angiography with a combined unit—initial experience. *Radiology.* 2001;220:499–505.

32. Soyer P. CT during arterial portography. *Eur Radiol.* 1996;6:349–357.

33. McTavish JD, Jinzaki M, Zou KH, et al. Multi-detector row CT urography: comparison of strategies for depicting the normal urinary collecting system. *Radiology.* 2002;225:783–790.

34. Hong KC, Freeny PC. Pancreaticoduodenal arcades and dorsal pancreatic artery: comparison of CT angiography with three-dimensional volume rendering, maximum intensity projection, and shaded-surface display. *AJR Am J Roentgenol.* 1999;172:925–931.

35. Tanikake M, Shimizu T, Narabayashi I, et al. Three-dimensional CT angiography of the hepatic artery: use of multi-detector row helical CT and a contrast agent. *Radiology.* 2003;227:883–889.